Rapid quantitative chemical mapping of surfaces with sub-2nm resolution

Chia-Yun Lai[1], Saverio Perri[2], Sergio Santos[1], Ricardo Garcia[3], Matteo Chiesa[1]

[1]Laboratory for Energy and NanoScience (LENS), Institute Center for Future Energy (iFES), Masdar Institute of Science and Technology, Abu Dhabi, UAE

[2]Instititute Center for Water and Environment (iWater), Masdar Institute of Science and Technology, Abu Dhabi, UAE

[3]Instituto de Ciencia de Materiales de Madrid, CSIC Sor Juana Inés de la Cruz, 28049 Madrid, Spain

Supplementary

Contents

Raw data and codes

All raw data and codes (produced via Matlab and the R language/R studio) can be found at https://github.com/BimodalHamakerMaps. A Readme.md file is also provided at the site with instructions of how to reproduce all the processed data and figures in this article from the raw data. Matlab and R should be installed in the system before running the scripts and R should be callable from the Matlab scripts by adding the R executable to the environment, i.e. under Windows this is done by adding the folder containing the R.exe and Rscript.exe files to the environment. The second mode amplitude was kept low throughout to approximately 0.1-0.3 nm while the set-point was always kept in the nm range. This is in agreement with most of the bimodal theory[1-3] that requires that $A_2 << A_1$.

Some of the raw parameters and processed data from the images employed in this work are also summarized below in the form of tables. The parameters provided are A_{sp}, A_0, A_r, $A_0{}^C$, d_{min}, R, and H_{IMG}. R is given in nm (nominal) and the rest of parameters in the International System of Units. Each raw corresponds to a bimodal image from Tables SI to SIV.

HOPG

A_{sp}	A_0	A_r	$A_o{}^C$	d_{min}	R	H_{IMG}
3.12E-09	4.77E-09	0.654109	0.28125	4.73E-10	10	1.58E-20
4.92E-09	5.3E-09	0.928434	0.3125	2.88E-10	10	9.04E-21
4.49E-09	5.3E-09	0.846415	0.3125	3.11E-10	10	1.46E-20
3.99E-09	5.3E-09	0.753132	0.3125	3.72E-10	10	2.29E-20
2.89E-09	3.18E-09	0.909245	0.1875	4.36E-10	10	6.99E-21
2.39E-09	3.18E-09	0.751478	0.1875	4.26E-10	10	1.32E-20
6.1E-09	7.53E-09	0.810019	0.44375	3.57E-10	10	3.16E-20
2.56E-09	2.87E-09	0.890814	0.2	4.26E-10	10	6.76E-21

2.4E-09	2.87E-09	0.835349	0.2	4.92E-10	10	9.84E-21
2.24E-09	2.87E-09	0.780199	0.2	5.47E-10	10	1.3E-20
2.08E-09	2.87E-09	0.725118	0.2	5.14E-10	10	1.31E-20
4.79E-09	5.31E-09	0.901544	0.37037	4.33E-10	10	1.76E-20
3.73E-09	5.31E-09	0.701638	0.37037	4.24E-10	10	3.4E-20
6.38E-09	6.91E-09	0.924279	0.481481	4.09E-10	10	2.43E-20
5.33E-09	6.91E-09	0.771982	0.481481	4.91E-10	10	6.14E-20
4.11E-09	5.22E-09	0.787211	0.351852	3.4E-10	10	1.8E-20
3.56E-09	5.22E-09	0.682466	0.351852	3.92E-10	10	2.64E-20
3.29E-09	5.22E-09	0.630083	0.351852	3.91E-10	10	2.68E-20
3.85E-09	5.22E-09	0.737417	0.351852	3.07E-10	10	1.35E-20
3.44E-09	3.95E-09	0.87032	0.266667	3.72E-10	10	1.19E-20
3.16E-09	3.95E-09	0.800369	0.266667	4.3E-10	10	1.96E-20
2.89E-09	3.95E-09	0.730849	0.266667	4.59E-10	10	2.43E-20
2.61E-09	3.95E-09	0.660899	0.266667	4.81E-10	10	2.82E-20
2.34E-09	3.95E-09	0.591631	0.266667	4.79E-10	10	2.89E-20
6.02E-09	6.59E-09	0.91357	0.444444	3.23E-10	10	1.58E-20
5.74E-09	6.59E-09	0.87157	0.444444	3.49E-10	10	2.21E-20
5.5E-09	6.59E-09	0.835474	0.444444	3.98E-10	10	3.22E-20
5.19E-09	6.59E-09	0.788282	0.444444	4.26E-10	10	3.98E-20
4.92E-09	6.59E-09	0.74657	0.444444	4.81E-10	10	5.32E-20
4.65E-09	6.59E-09	0.705161	0.444444	4.92E-10	10	5.73E-20
4.37E-09	6.59E-09	0.663449	0.444444	5.05E-10	10	6.25E-20
4.1E-09	6.59E-09	0.621706	0.444444	5.16E-10	10	6.62E-20
6.57E-09	7.41E-09	0.886028	0.5	3.55E-10	10	2.27E-20
6.29E-09	7.41E-09	0.849315	0.5	3.96E-10	10	3.33E-20
6.02E-09	7.41E-09	0.811739	0.5	4.3E-10	10	4.29E-20
5.75E-09	7.41E-09	0.77516	0.5	4.58E-10	10	5.28E-20
5.47E-09	7.41E-09	0.737961	0.5	4.84E-10	10	6.19E-20
5.19E-09	7.41E-09	0.700519	0.5	4.99E-10	10	6.77E-20
4.92E-09	7.41E-09	0.663644	0.5	5.12E-10	10	7.31E-20
4.65E-09	7.41E-09	0.62681	0.5	5.21E-10	10	7.68E-20
4.37E-09	7.41E-09	0.589773	0.5	5.23E-10	10	7.8E-20
4.1E-09	7.41E-09	0.552655	0.5	5.36E-10	10	8.28E-20
8.93E-09	1.17E-08	0.766089	0.485833	3.81E-10	10	6.69E-20
1.06E-08	1.33E-08	0.799932	0.552083	4.15E-10	10	8.86E-20
8.12E-09	1.33E-08	0.612845	0.552083	5.42E-10	10	1.66E-19
1.06E-08	1.43E-08	0.741377	0.59625	5.56E-10	10	1.77E-19
8.46E-09	1.43E-08	0.59144	0.59625	6.56E-10	10	2.53E-19
4.44E-09	5.23E-09	0.849101	0.37037	2.74E-10	10	1.2E-20
3.92E-09	5.23E-09	0.749082	0.37037	3.14E-10	10	1.9E-20

3.66E-09	5.23E-09	0.699101	0.37037	3.32E-10	10	2.24E-20
3.13E-09	5.23E-09	0.599101	0.37037	3.53E-10	10	2.64E-20
6.27E-09	6.8E-09	0.922356	0.481481	3E-10	10	1.4E-20
5.23E-09	6.8E-09	0.76851	0.481481	4.24E-10	10	4.45E-20
4.18E-09	6.8E-09	0.61462	0.481481	4.88E-10	10	6.43E-20

Table SI. Experimental and processed data from the 54 images obtained on HOPG in this work to validate the theory and discussed in the main text. This data has been employed to produce Fig. 2. All values are given employing the International System of Units.

mica

A_{sp}	A_0	A_r	A_o [C]	d_{min}	R	H_{IMG}
4.89E-09	5.43E-09	0.90046	0.322581	4.94E-10	10	2.96E-20
5.97E-09	6.52E-09	0.916897	0.387097	4.85E-10	10	3.36E-20
5.43E-09	6.52E-09	0.833364	0.387097	5.22E-10	10	4.87E-20
5.16E-09	6.52E-09	0.791268	0.387097	5.33E-10	10	5.46E-20
6.89E-09	8.15E-09	0.846495	0.483871	5.65E-10	10	7.48E-20
5.03E-09	5.59E-09	0.89973	0.286111	4.57E-10	10	1.89E-20
3.93E-09	4.34E-09	0.904581	0.222222	4.14E-10	10	1.27E-20
3.52E-09	3.8E-09	0.926809	0.194444	4.28E-10	10	1.02E-20
2.01E-09	2.17E-09	0.923849	0.111111	4.93E-10	10	6.92E-21
7.43E-09	1.09E-08	0.683847	0.5125	6.68E-10	10	1.59E-19
9.03E-09	1.09E-08	0.831496	0.5125	5.3E-10	10	8.22E-20
9.97E-09	1.22E-08	0.818097	0.575	6.03E-10	10	1.28E-19
9.97E-09	1.22E-08	0.818097	0.5625	5.98E-10	10	1.28E-19
1.06E-08	1.22E-08	0.87	0.5625	5.38E-10	10	9.07E-20
1.17E-08	1.33E-08	0.882611	0.625	4.43E-10	10	4.44E-20
9.79E-09	1.33E-08	0.738687	0.625	7.05E-10	10	2E-19

Table SII. Experimental and processed data from the 16 images obtained on mica in this work to validate the theory and discussed in the main text. All values are given employing the International System of Units.

PFDA

A_{sp}	A_0	A_r	A_o [C]	d_{min}	R	H_{IMG}
3.74E-09	4.95E-09	0.75497	0.583679	2.87E-10	10	9.97E-21
4.84E-09	5.4E-09	0.8955	0.636792	3.22E-10	10	1.02E-20
5.92E-09	6.46E-09	0.917395	0.761321	3.7E-10	10	2.12E-20
4.24E-09	4.3E-09	0.985874	0.507547	5.05E-10	10	2.5E-20
4.01E-09	5.3E-09	0.755925	0.625	2.65E-10	10	1.31E-20
3.72E-09	5.3E-09	0.701491	0.625	2.93E-10	10	1.64E-20
3.53E-09	5.3E-09	0.665396	0.625	2.73E-10	10	1.52E-20
3.33E-09	5.3E-09	0.628981	0.625	2.88E-10	10	1.7E-20
3.74E-09	4.95E-09	0.75497	0.583679	2.87E-10	10	9.97E-21

Table SIII. Experimental and processed data from the 9 images obtained on PFDA in this work to validate the theory and discussed in the main text. All values are given employing the International System of Units.

calcite

A_{sp}	A_0	A_r	A_o [C]	d_{min}	R	H_{IMG}
5.80E-09	7.04E-09	8.24E-01	5.33E-01	4.30E-10	10	2.98E-20
3.20E-09	4.10E-09	7.80E-01	3.11E-01	4.60E-10	10	1.92E-20
6.66E-09	8.25E-09	8.07E-01	6.25E-01	4.80E-10	10	4.74E-20
5.71E-09	8.25E-09	6.92E-01	6.25E-01	5.50E-10	10	7.30E-20

5.60E-09	6.60E-09	8.48E-01	5.00E-01	3.90E-10	10	2.10E-19

Table SIV. Experimental and processed data from the 5 images obtained on calcite in this work to validate the theory and discussed in the main text. All values are given employing the International System of Units.

A_c determination

In the main text, we have defined A_c as the minimum (or critical) free amplitude for a cantilever to experience bi-stability. The use of A_c to the determine effect tip radius has been first reported in 2012[4] stating that there exists a specific power-law relationship between A_c and effective tip radius. Here we showed the steps of how to determine A_c using amplitude or phase versus distance (APD) curves.

1) Set the drive frequency at the natural frequency of oscillation and a small value of A_{01} (4-5 nm), a trigger point in the range of 0.5-2 nm. Experimental APD curves are acquired now.
2) Inspecting the APD curves that whether the attractive regime only prevails throughout or the repulsive regime has been reached. If only the attractive regime was observed, the value of A_{01} has to be increased.
3) As A_{01} is increased, a value of A_{01} is eventually reached and a transition to the repulsive regime is observed. This can be concluded by checking the APD curves where there is an abrupt jump in the curves.
4) As A_c exists as a range of A_{01} values, we take the minimum value as our critical amplitude to determine the effective tip radius.

Force measurements

III.A Force reconstruction from force profiles

Experimental force F_{ts} versus d profiles were obtained from raw amplitude A ($A \equiv A_1 \equiv A_{sp}$) versus phase ϕ ($\phi=\phi_1$) curves (APD curves) obtained on a sample. These curves were converted into F_{ts} versus d profiles by exploiting the Sader-Jarvis-Katan (SJK) formalism (conservative forces) that consists of a series of integrals to be solved per point (d) as follows (see literature for details[5-7]):

$$F(d) = 2k\int_{u=d}^{u=\infty}\left[\left(1+\frac{A^{1/2}(u)}{8\sqrt{\pi(u-d)}}\right)\Omega(u)-\frac{A^{3/2}(u)}{\sqrt{2(u-d)}}\frac{d\Omega(u)}{du}\right]du \qquad \text{(S1)}$$

where Ω is the normalized frequency shift expressed by:

$$\Omega(d) = \left[1+\frac{A_0}{QA}\cos(\Phi(d))\right]^{\frac{1}{2}} - 1 \qquad \text{(S2)}$$

where Q is the quality factor and A_0 is the free amplitude. All the experiments have been carried out with a Cypher AFM from Asylum Research and standard OLYMPUS cantilevers (AC160TS -40 N/m, and AC240TS – 2 N/m). Since it is well-known that the tip radius *R* significantly affects the interaction force between the tip and the surface[4], R was constantly monitored *in situ* during the experiments. The initial value of R was assumed to agree with the nominal values provided by the manufacturer, i.e. $R \approx 10$ nm.

The experimental steps to take AFM-APD curves are:

1) A sample was mounted for standard AFM (Cypher AFM from Asylum Research) data acquisition.

2) A new AFM cantilever (OLYMPUS AC160TS with k=40N/m and Q factor≈ 500 or OLYMPUS AC240TS with k=2 N/m and Q factor≈ 100) was mounted on the AFM cantilever holder.

3) The value of R was monitored[4] by acquiring standard[8] APD curves and these were used to compute the critical amplitude[9] A_c value in raw Volt units[4]. The initial value of R was assumed to agree with the nominal values provided by the manufacturer, i.e. R ≈ 10 nm. Provided A_c did not change for a given sample during the experiments, we assumed that R remained constant.

4) Approximately 1000-2000 APDs were acquired immediately after computing the value of R for each tip.

5) The raw APD curves were then converted into F_{ts} versus distance d profiles as those presented in Figs. S1a for HOPG and S1b for PFDA. In Fig. S1 the raw data is shown in red dots and the Hamaker fits in blue lines. Each APD produces an F_{ts} versus d profile. We defined d=0 at minima in F_{ts}, i.e. when F_{ts} coincides with the force of adhesion F_{AD}.

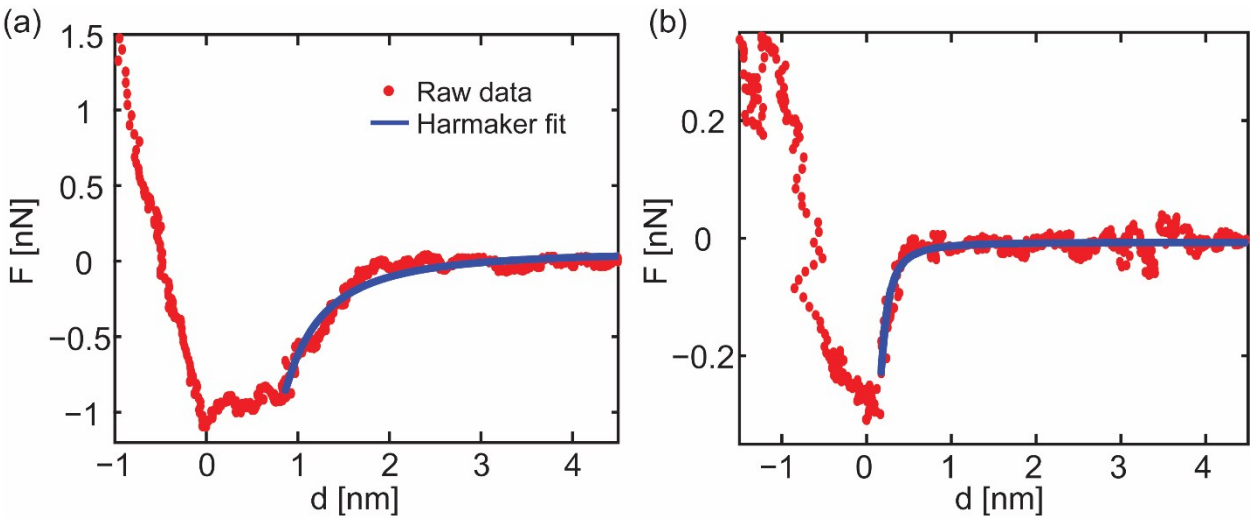

Fig. S1 Raw experimental (red dots) HOPG and b) PFDA force profiles and (blue lines) best fits obtained by employing standard linear regression on the raw data and the model in (1) for β=0.9.

III.B Computation of the Hamaker coefficient from force versus d data

Force profiles (see Fig. S1) have been further parameterized in this work (see scheme of Fig. S2) in terms of the minima in force, i.e. force of adhesion F_{AD}, via a β parameter such that $F_{ts} = \beta F_{AD}$, where β=0.1, 0.15, …, 0.9. Then linear regression on the raw force profiles was performed for data sets including data from the largest values of d to the values of d at which β=0.1, 0.15, …, 0.9 correspondingly. The H value resulting from these force curves is termed H_{FIT} in order to differentiated from the value of H predicted by the Lifshitz theory (H_{LT}) and the value recovered from bimodal images (H_{IMG}). It was found that the value of H_{FIT} depended on β as shown in Fig. S3a (HOPG) and Fig. S4a (PFDA).

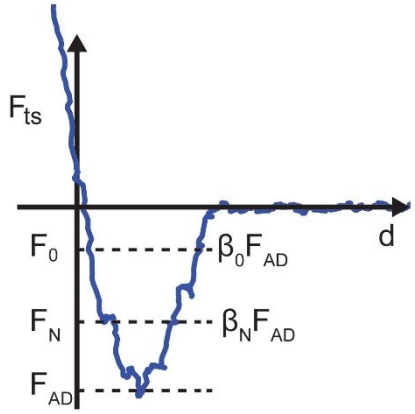

Fig. S2

Figure S3: HOPG

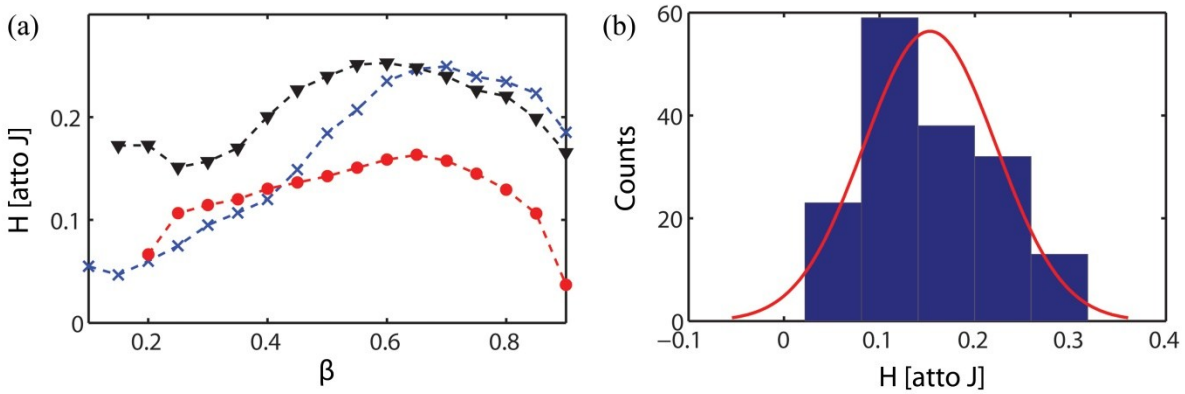

In Fig. S3a the value of H_{FIT} resulting from fitting force versus distances profiles from three different tips on a HOPG are shown with the help of triangles, crosses and circles as a function of β. Each point in the figure further corresponds to the average obtained for a given tip over ~100-1000 force curves. The data is further presented in Fig. S3b in the form of a histogram that shows that the mean value of HFIT for all β β is $H_{FIT} \approx 0.15$ atto J as reported in the main text.

Figure S4: PFDA

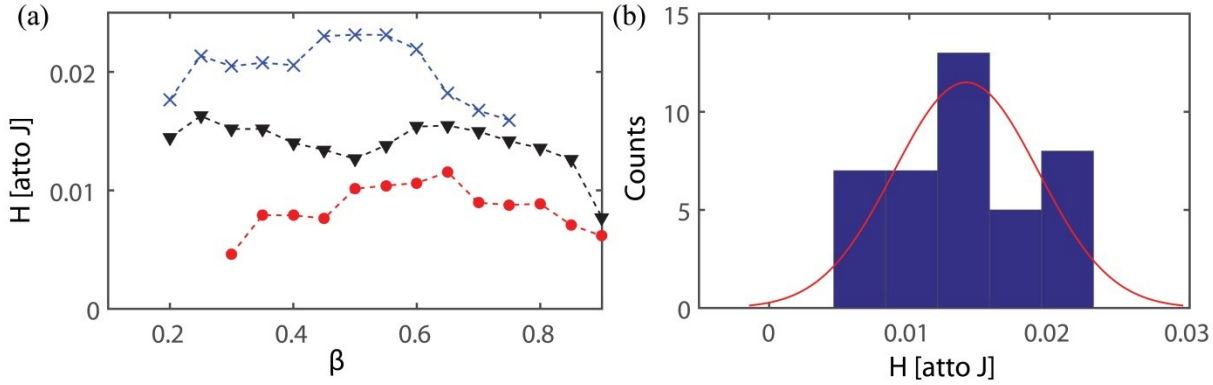

In Fig. S4a the value of H_{FIT} resulting from fitting force versus distances profiles from three different tips on a PFDA sample are shown with the help of triangles, crosses and circles as a function of β as in Fig. S3. Each point in the figure also further corresponds to the average obtained for a given tip over ~100-1000 force curves. The full range of data (5 tips) is further presented in Fig. S4b in the form of a histogram that shows that the mean value of H_{FIT} for all β is $H_{FIT} \approx 0.014$ atto J as reported in the main text.

Figure S5: mica

The values for H_{FIT} for the mica sample were computed similarly and data is shown in Fig. S5 for a tip with R≈10 nm (data points averaged over 1000 force curves) and R≈40 nm in crosses and circles respectively. The mean value is, in both cases, $H_{FIT} \approx 0.1$ atto J as stated in the main text.

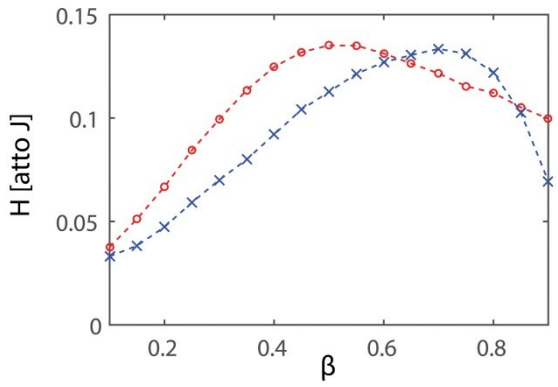

Fig. S5 Hamaker values obtained from force versus distance profiles on a mica sample as a function of β for a tip with radius R≈10 nm (crosses) and a tip with radius R≈40 nm (circles).

Derivation of the bimodal expressions for Hamaker and d_{min}

A General Virial expression for the van der Waals force

The bimodal theory[1, 2, 10-12] states that the virial V for modes 1 and 2 can be obtained directly from observables via (3) (reproduced below for clarity):

$$V_m(d_{\min}) \equiv \frac{1}{T}\oint F_{ts} z_m dt = -\frac{A_m(d_{\min})k_m A_{0m}}{2Q_m}\cos\phi_m(d_{\min}) \qquad \text{(S3)}$$

By combining (S3) and (1), where (1) is the model for the force employed in this work as described in the main text, it can be shown[13] that

$$V_1(H,d_{\min}) = \frac{1}{T}\oint -\frac{RH}{6d^2} z_1 dt \approx \frac{RH}{6A_1}\left[\left(\frac{d_{\min}+A_1}{A_1}\right)^2 - 1\right]^{-3/2} \tag{S4}$$

Combining (S3) and (S4) one equation with 2 unknowns, i.e. d_{min} and H, results.

A second equation can be derived from the second mode Virial. On the other hand, the second virial should be expressed in terms of the tip position of the first mode z_1 in order to make the calculations tractable. This simplification was proposed by Kawai et al.[3] and the approximations discussed in detail by Aksoy and Atalar [1] and others[2, 14]. Assuming that during a full first mode cycle the derivative is an even function of position, the simplifications proposed in the literature, assuming the model in (1), are equivalent to

$$V_2(H,d_{\min}) = \frac{1}{T}\oint -\frac{RH}{6d^2} z_2 dt \approx \frac{RH}{6\pi} A_2^2 \int_{-1}^{1} \frac{du}{\left[d_{\min}+A_1(1+u)\right]^3\sqrt{1-u^2}} \tag{S5}$$

The above results from combining [3, 15]

$$\frac{1}{T}\oint \frac{\partial F_{ts}}{\partial z} dt \approx -2k_2 \frac{\Delta f_2}{f_{02}} \tag{S6}$$

and[2, 11]

$$V_2 \approx -k_2 A_2^2 \frac{\Delta f_2}{f_{02}} \tag{S7}$$

from which the second mode virial can be rewritten as

$$V_2 \approx \frac{A_2^2}{2T}\oint \frac{\partial F_{ts}}{\partial z} dt \tag{S8}$$

The expression in (S5) results from inserting (1) into (S8) and assuming harmonic motion as usual, i.e. $z \approx A_1\cos(\omega_1 t-\phi_1)$

III.B Solution of second mode virial for the van der Waals force

The objective is to solve the integral in (S8) that can be written as

$$I(a,b)=\int_{-1}^{1}\frac{du}{\left[a+b(1+u)\right]^3\sqrt{1-u^2}} \tag{S9}$$

where $a=d_{min}$ and $b=A_1$.

Analytical solution of (S9)

After a few changes of variable the solution of (S9) can be found in close form as

$$I \approx \frac{\left(2a^2+4ab+3b^2\right)ArcTan\left[\frac{4.47\times10^7\sqrt{a}}{\sqrt{a+2b}}\right]}{2a^{5/2}(a+2b)^{5/2}}+$$
$$-\frac{4.47\times10^7 b(8\times10^{15}a^2+1+ab(10^{16}+11)+6b^2)}{2a^2(a+2b)^2(a+2\times10^{15}b)^2} \tag{S10}$$

Hereafter equation (S10) is considered the analytical solution of (S9). Since (S10) is cumbersome, an approximation is sought.

Approximate solution of (S10)

Considering that

$$ArcTan[\frac{4.47 \times 10^7 \sqrt{a}}{\sqrt{a+2b}} \approx 1.571 \quad \text{(S11)}$$

Furthermore, from dimensional analysis, and neglecting the second term of (S10)

$$\frac{1{,}571(2a^2+4ab+3b^2)}{2a^{5/2}(a+2b)^{5/2}} \quad \text{(S12)}$$

Furthermore, whenever b>>a, it follows that

$$I \approx \frac{0.833148}{\sqrt{a^5 b}} \quad \text{(S13)}$$

Or

$$I(d_{\min}, A_1) \approx \frac{0.83}{\sqrt{d_{\min}^5 A_1}} \quad \text{(S14)}$$

Hereafter (S13), or equivalently, (S14), is considered the approximate solution to (S9) and (S10) and it is simple enough for the purpose of this work.

Comparison between the numerical integration and the analytic solution (S10) and the approximate solution (S13)

As shown in the example in Fig. S6, the numerical solution coincides with the analytical solution in (S10) with errors smaller than 1% as compared to numerical integration of (S9). In the figure, the x axis is $b=A_1$ and $a=d_{min}$ has been set to 1nm. The physical implication is that for the range of set point amplitudes explored here, i.e. 1- 10 nm, the analytical solution coincides with the numerical integration of (S9). These results have practical use since in attractive bimodal AFM the set point amplitude A1 or Asp lies in such range. See for example our Table I in the main text and other works in the literature [15-18].

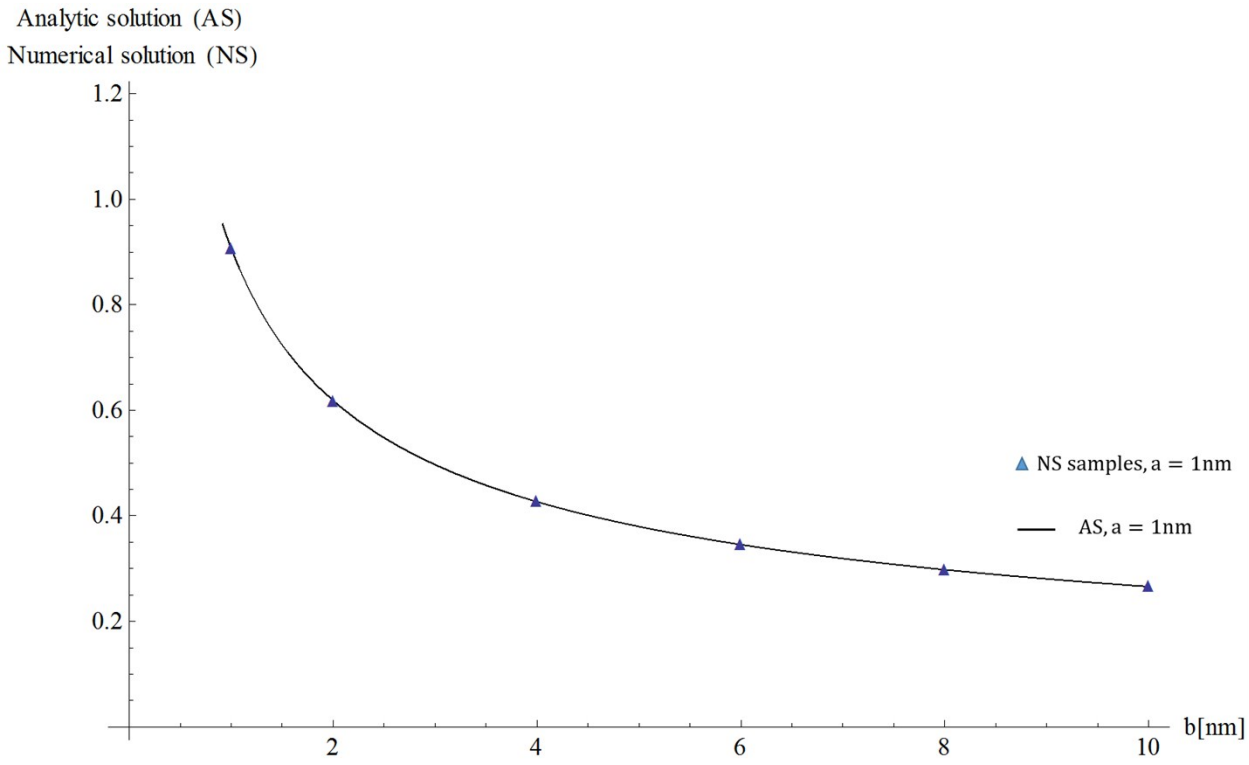

Fig. S6. Comparison between numerical integration of (S9) and the analytical solution in (S10) and as a function of b, with a=1nm.

The next two figures (Fig. S7 and Fig. S8) show the results of the analytic solution in (S10) that, again, coincides with numerical integration of (S9) with errors smaller than 1% and the approximate solution in (S13). In Fig. S7 b ≡ A_1=10 nm and a≡d_{min} is varied from 0.25 nm to 1 nm. The approximation in (S13) produces errors smaller than 1%. An extreme case of operation is presented in Fig. (S8) for which b ≡ A_1=0.5 nm and a≡d_{min} varies from 0.25 to 1 nm. In this extreme case errors are still predicted to be smaller than 10%.

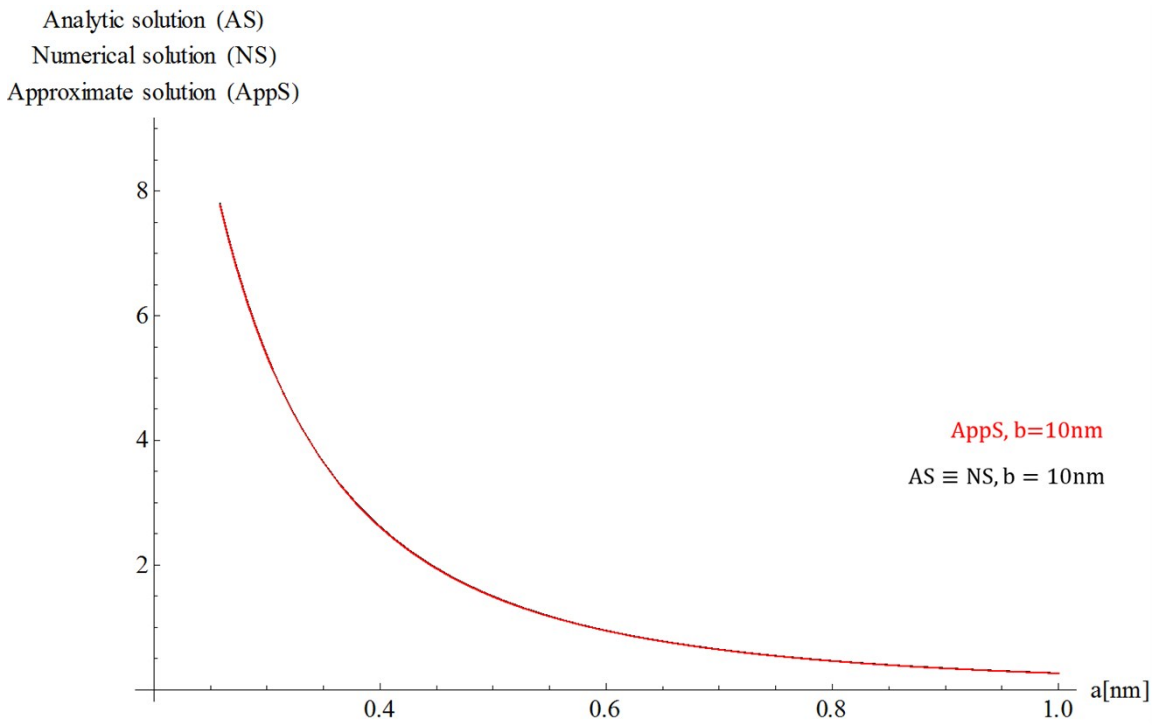

Fig. S7- Analytical-numerical solution compared with the approximation in (S13) for b=10nm.

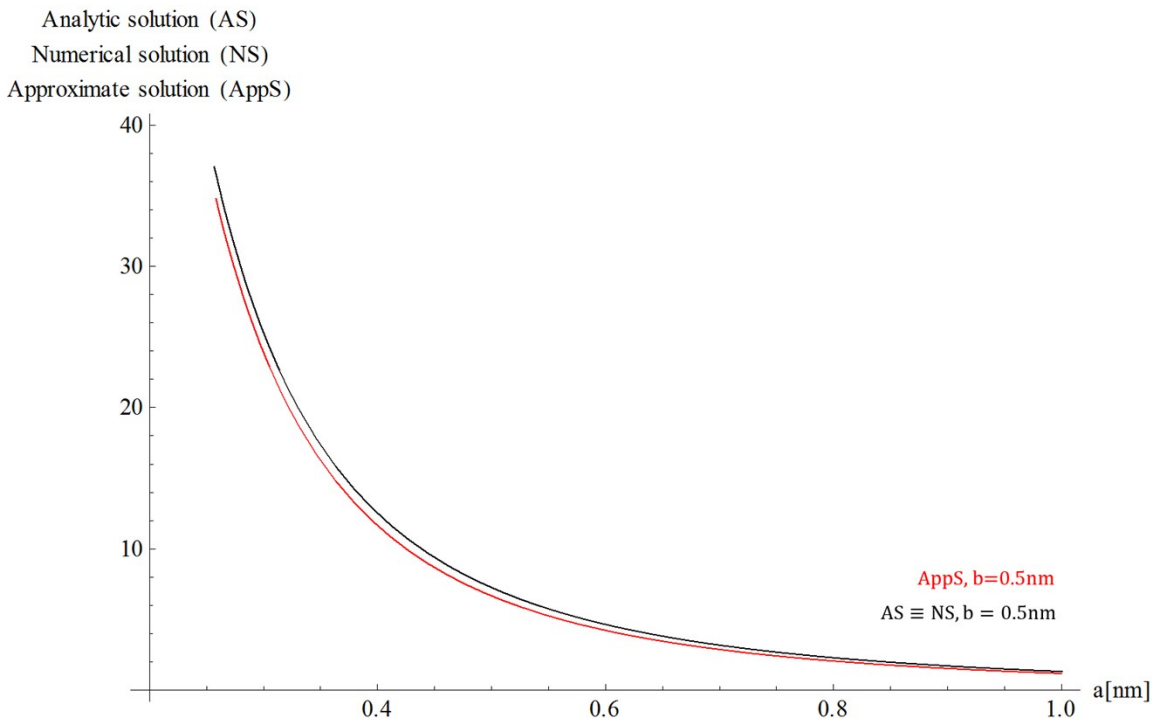

Fig. S8 Analytical-numerical solution compared with the approximated solution given by equation in (S13) with b=0.5nm.

Figs.S9 and S10 show the comparison between the numerical solution as a function of b when is a= 0.2nm and a= 1nm respectively.

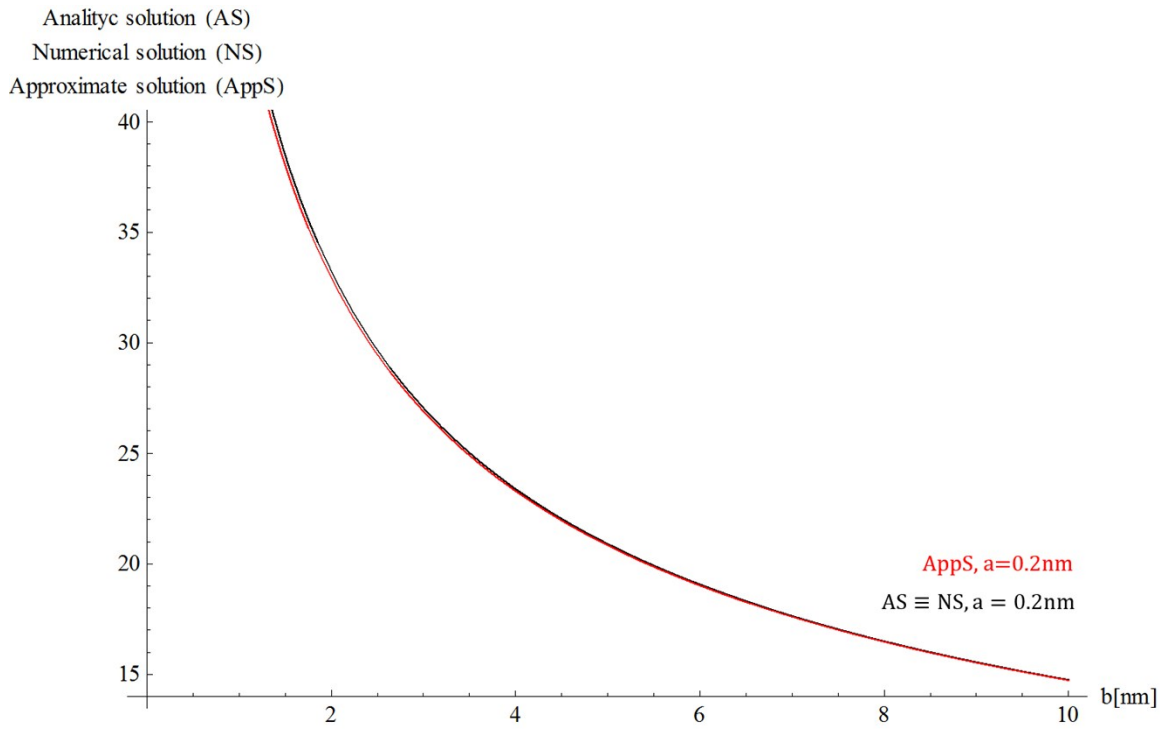

Fig. S9 Analytical-numerical solution compared with the approximated solution given by equation in (S13) with a=0.2 nm.

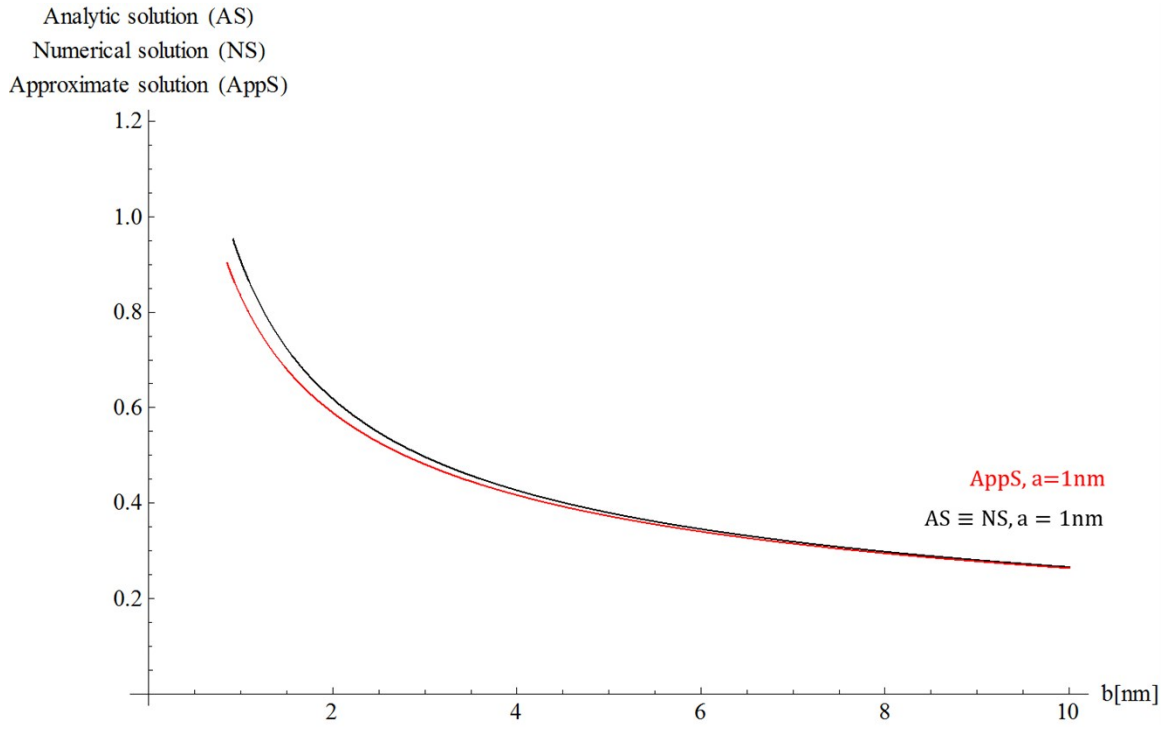

Fig. S10 Analytical-numerical solution compared with the approximated solution given by equation in (S13) with a=1 nm.

In summary, the error of the approximation in (S13) is always lower than 5% except in cases where $a>b$. In such cases the maximum error reaches 11% the range of parameters explored in the figures above. In principle, provided $a>b$ the error from (S13) tends to zero. The practical result here is that one can employ the approximation in (S13) provided the oscillation amplitude $A_1=A_{sp}$, i.e. b, is larger than the minimum distance of approach d_{min}, i.e. a. In any case, this is true in all our examples since, as corroborated from the force profiles, the decay length of the van der Waals forces (see Fig. S1) is always in the order of 0.5-2 nm while oscillation amplitudes employed in this work for Asp ar4e always larger than 2 nm.

Linear Regression (Fig. 2)

For Fig. 2 the data from H_{IMG} from Table SI for the HOPG sample has been employed to get best fits employing the following models

Fig. 2a

$$H_{IMG} = \theta_0 + \theta_1 A_r \tag{S15}$$

From which the values provided in Table SIV resulted:

θ_0	SE(θ_0)	θ_1	SE(θ_1)	ρ
0.21	0.05	-0.21	0.07	0.13

Table IV Coefficients resulting from linear regression where only one regressor, associated with the normalized set point $A_r=A_{sp}/A_0$ is assumed. SE stands for the Standard error associated with the regressor.

Fig. 2b

$$H_{IMG} = \theta_0 + \theta_1 \left[A_0^C\right] \tag{S16}$$

θ_0	SE(θ_0)	θ_1	SE(θ_1)	ρ
-0.01	0.01	0.66	0.06	0.68

Table V Coefficients resulting from linear regression where only one regressor, associated with the normalized critical amplitude $A_0^C=A_c/A_0$ is assumed.

Fig. 2c

$$H_{IMG} = \theta_0 + \theta_1 A_r + \theta_2 \left[A_0^C\right] \quad \text{(S17)}$$

From which the values provided in Table SVI below resulted:

θ_0	SE(θ_0)	θ_1	SE(θ_1)	θ_2	SE(θ_2)	ρ
0.03	0.03	-0.17	0.03	0.64	0.05	0.77

Table VI Coefficients resulting from linear regression where two regressors associated with the normalized set point $A_r=A_{sp}/A_0$ and normalized critical amplitude $A_0^C=A_c/A_0$ are assumed.

The physical interpretation of the regressors is that H_{IMG} depends linearly on the regressor with the coefficients of linearity θ provided in the tables. From the main text and Fig. 2 it was found that provided $A_0^C \approx 0.5\text{-}0.6$ the value of H computed in the bimodal images was in agreement with the Lifshitz theory and the fitting from force profiles computed as described in section 2 (Force measurements) above.

The two phases of calcite

In the main text we discuss the two regions probed from force curves obtained from amplitude and phase versus distance APD data. Two examples of force profiles, one on each region, are shown in Fig. S11. Hundreds of data points were obtained for each region and the regions could

be distinguished directly from the raw phase 1 θ_1, phase 2 θ_2 or amplitude 2 A_2 data as shown in Fig. S12.

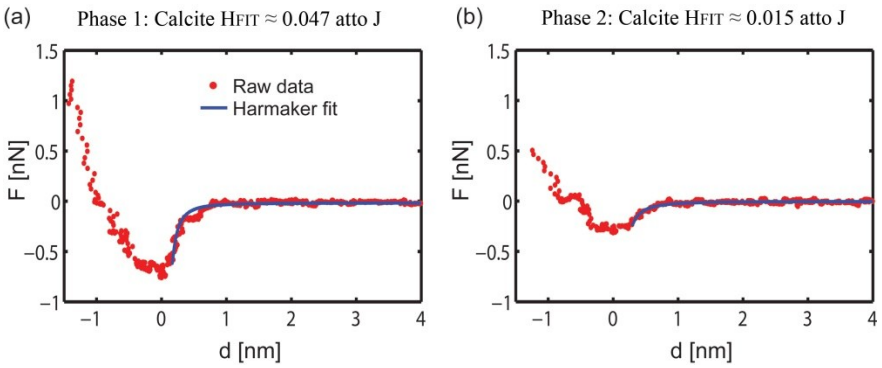

Fig. S11. Force profiles and fit of (1) for the two phases of calcite.

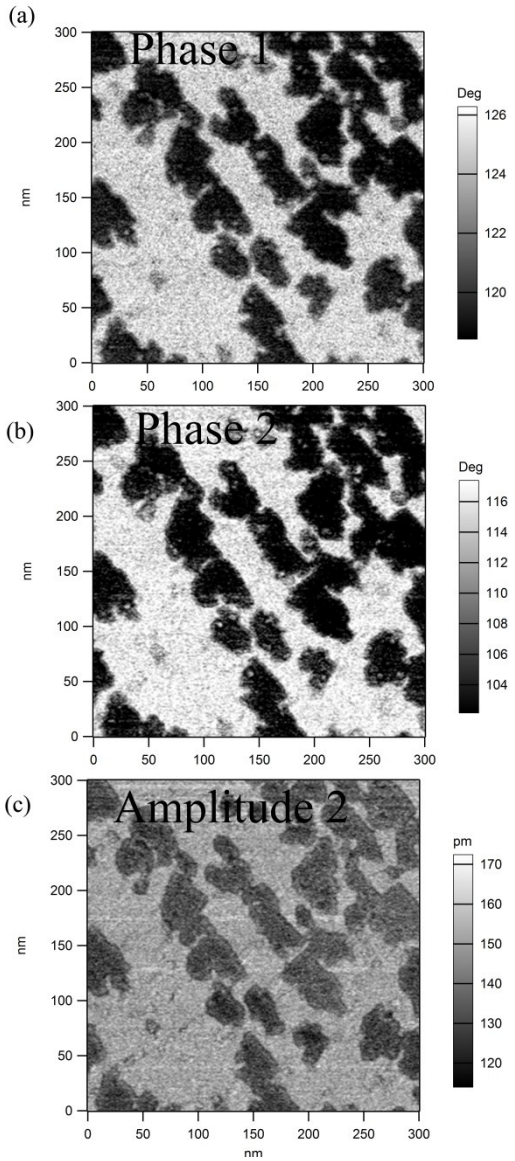

Fig. S12 Raw phases (a) and (b) and second amplitude (c) for a calcite sample.

Derivation of main expressions in the text (4) and (5)

Combining (S5) and (S14)

$$V_2(H, d_{\min}) \approx \frac{RH}{6\pi} A_2^2 \frac{0.83}{\sqrt{d_{\min}^5 A_1}} \tag{S18}$$

Expression (S18) is the second equation necessary with the two unknowns required, i.e. d_{min} and H, that combined with (S4) results in a system of two equations in two unknowns. Solving for d_{min} the solution can be expressed as

$$d_{\min} + b d_{\min}^{2/3} + c = 0 \tag{S19}$$

in accordance with (4) in the main text. The coefficients b and c are found to be

$$b = -\left[\frac{3\pi k_2 A_{02} Q_1 \cos\phi_2}{0.83 k_1 A_{01} Q_2 \cos\phi_1}\right]^{2/3} \frac{A_1}{(A_2)^{2/3}} \tag{S20}$$

$$c = 2A_1 \tag{S21}$$

The zeros of (S19) were found here in Matlab with the help of the standard fzero function and initial values were assumed to lie in the 1 nm range.

Provided dmin was found for a given pixel in the image, the solution for H in terms of V_1 was trivial ($A_{sp}=A_1$)

$$H = -\frac{A_1^2 k_1 A_{01} \cos\phi_1}{RQ_1}\left[\left(\frac{d_{\min}+A_1}{A_1}\right)^2 - 1\right]^{3/2}$$

and in terms of V_2

$$H = -\frac{3\pi k_2 A_{02} \cos\phi_2}{0.83RQ_2A_2}\sqrt{d_{\min}^5 A_1}$$

When no solution for (S19) were found H was not computed. Errors resulted in some pixels for which dmin was not found. Images for which 10% of pixels produced errors were discarded. In our case, this resulted mostly when working outside resonance, i.e. this formalism is based on the AFM being operated at the two modal resonances.

1. Aksoy, M.D. and A. Atalar, *Force spectroscopy using bimodal frequency modulation atomic force microscopy.* Physical Review B, 2011. **83**(7): p. 075416.

2. Herruzo, E.T. and R. Garcia, *Theoretical study of the frequency shift in bimodal FM-AFM by fractional calculus.* Beilstein Journal of Nanotechnology, 2012. **3**: p. 198-206.
3. Kawai, S., et al., *Systematic Achievement of Improved Atomic-Scale Contrast via Bimodal Dynamic Force Microscopy* Physical Review Letters, 2009. **103**: p. 220801-220804.
4. Santos, S., et al., *A method to provide rapid in situ determination of tip radius in dynamic atomic force microscopy.* Review of Scientific Instruments, 2012. **83**(4): p. 043707.
5. Sader, J.E. and S.P. Jarvis, *Accurate formulas for interaction force and energy in frequency modulation force spectroscopy.* Applied physics letters, 2004. **84**(10): p. 1801-1803.
6. Katan, A.J., M.H. Van Es, and T.H. Oosterkamp, *Quantitative force versus distance measurements in amplitude modulation AFM: a novel force inversion technique.* Nanotechnology, 2009. **20**(16): p. 165703.
7. Santos, S., et al., *Size Dependent Transitions in Nanoscale Dissipation.* Journal of Physical Chemistry C, 2013. **117**(20): p. 10615-10622.
8. Ziegler, K.J., et al., *Bistable nanoelectromechanical devices.* Applied physics letters, 2004. **84**: p. 4074.
9. Santos, S., et al., *A method to provide rapid in situ determination of tip radius in dynamic atomic force microscopy.* Review of Scientific Instruments, 2012. **83**: p. 043707-043717.
10. Lozano, J.R. and R. Garcia, *Theory of Multifrequency Atomic Force Microscopy.* Physical Review Letters, 2008. **100**: p. 076102-076105.
11. Lozano, J.R. and R. Garcia, *Theory of phase spectroscopy in bimodal atomic force microscopy.* Physical Review B, 2009. **79**(1): p. 014110.
12. Santos, S., *Phase contrast and operation regimes in multifrequency atomic force microscopy.* Applied Physics Letters, 2014. **104**: p. 143109-143113.
13. Paulo, A.S. and R. Garcia, *Tip-surface, amplitude, and energy dissipation in amplitude-modulation (tapping mode) force microscopy.* Physical Review B, 2001. **64**: p. 193411-193414.
14. Santos, S., *Theory of small amplitude bimodal atomic force microscopy in ambient conditions* arxiv.org/pdf/1401.6687, 2014.
15. Martinez-Martin, D., et al., *Noninvasive protein structural flexibility mapping by bimodal dynamic force microscopy.* Physical review letters, 2011. **106**(19): p. 198101.
16. Herruzo, E.T., A.P. Perrino, and R. Garcia, *Fast nanomechanical spectroscopy of soft matter.* Nature Communications, 2014. **5**: p. 10.1038/ncomms4126.
17. Kiracofe, D., A. Raman, and D. Yablon, *Multiple regimes of operation in bimodal AFM: understanding the energy of cantilever eigenmodes.* Beilstein Journal of Nanotechnology, 2013. **4**: p. 385–393.
18. An, S., et al., *Energy Transfer Between Eigenmodes in Multimodal Atomic Force Microscopy.* Nanotechnology, 2014. **25**: p. 475701-475711.